

**Magnetic resonance study of H atoms in thin films of H<sub>2</sub> at temperatures below 1 K**J. Ahokas,<sup>1,\*</sup> O. Vainio,<sup>1</sup> S. Novotny,<sup>1</sup> J. Järvinen,<sup>1,2</sup> V. V. Khmel'ko,<sup>2,3</sup> D. M. Lee,<sup>2,3</sup> and S. Vasiliev<sup>1</sup><sup>1</sup>*Wihuri Physical Laboratory, Department of Physics and Astronomy, University of Turku, 20014 Turku, Finland*<sup>2</sup>*Laboratory of Atomic and Solid State Physics, Cornell University, Ithaca, New York 14850, USA*<sup>3</sup>*Department of Physics and Astronomy, Texas A&M University, College Station, Texas 77843, USA*

(Received 21 October 2009; revised manuscript received 29 January 2010; published 17 March 2010)

We present an experimental study of H atoms embedded in thin films of solid H<sub>2</sub> at temperatures below 1 K. H<sub>2</sub> films up to 50 nm thick were first grown as a result of slow recombination of atomic hydrogen gas on the sample cell walls. If the recombination occurred in three-body atomic collisions in the gas phase, small concentrations of atoms could be captured inside the films during the film deposition. As a second method of generating atomic populations inside the H<sub>2</sub> films, we used a direct dissociation by a low power rf discharge in the sample cell. With this latter method, we achieved record high atomic concentrations exceeding  $2 \times 10^{19} \text{ cm}^{-3}$ . The samples were characterized by means of magnetic resonance: electron spin resonance (ESR) and electron-nuclear double resonance (ENDOR) in a magnetic field of 4.6 T. We observed density-dependent broadening and shifts of the ESR lines due to the dipolar interactions, and resolved these effects for like and unlike atoms. Relaxation of the relative hyperfine populations was measured as a function of temperature for H in H<sub>2</sub> films grown on different substrates. For H<sub>2</sub> films on Mylar substrates, the relative equilibrium populations of the two lowest hyperfine states of H were found to deviate substantially from the prediction of Boltzmann statistics. We also found two narrow lines in the ENDOR spectra of H in H<sub>2</sub> films shifted to the red from the position for free atoms. This indicates two possible substitutional positions of the atoms in H<sub>2</sub> matrices, both characterized by very homogeneous crystalline fields.

DOI: [10.1103/PhysRevB.81.104516](https://doi.org/10.1103/PhysRevB.81.104516)

PACS number(s): 67.80.fh, 67.80.dj, 76.30.-v

**I. INTRODUCTION**

One of the main goals in the matrix stabilization of atoms and free radicals is to isolate and inhibit the recombination of substances highly reactive under normal conditions.<sup>1</sup> Matrix stabilized atoms remain nearly inert at low temperatures and can only interact through quantum-mechanical tunneling, restricting their chemical reactions with atoms located at other sites. This opens up a new area of research in the field of quantum chemistry. At low enough temperatures, stabilizing high densities of impurities in a solid matrix also holds the promise of observing collective quantum phenomena such as Bose-Einstein condensation (BEC) and superfluidity.<sup>2</sup> Recently such a phenomenon has been found in solid <sup>4</sup>He, where anomalous rotational inertia<sup>3</sup> was identified with supersolid behavior. Owing to their small masses, hydrogen atoms in solid H<sub>2</sub> present one of the simplest cases of matrix stabilized atoms and thus allow investigation of the most fundamental quantum effects. This has motivated our studies, by focusing the main objective of our work on reaching the highest possible atomic densities at the lowest possible temperatures in order to initiate collective quantum phenomena leading to Bose-Einstein condensation or supersolidity.<sup>4</sup> We expected that these phenomena should reveal themselves in magnetic resonance spectroscopy which was used as the main diagnostic tool in our studies.

In this paper, we present a detailed description of our studies of atomic hydrogen in films of solid H<sub>2</sub> at temperatures below 1 K. The methods of creating the films of solid H<sub>2</sub> originate from studies of spin-polarized atomic hydrogen in the gas phase (H↓).<sup>5,6</sup> The main difference between the technique applied here and conventional methods of creating samples with matrix isolated atoms is the very slow growth

rate of the solid films ( $\approx 1$  molecular layer per hour) and very low energy released during this process. This allows creation of samples at temperatures  $\sim 0.5$  K with the possibility of further cooling to ultralow temperatures in a cell cooled by a dilution refrigerator. We found that the recombination of the hydrogen atoms into molecules is strongly suppressed below 1 K, even at very high densities.<sup>5,7</sup> Due to this feature, we increased by a factor of 3, the maximum H atom concentration to  $n \approx 2 \times 10^{19} \text{ cm}^{-3}$  reached in the system of H in H<sub>2</sub>.<sup>7</sup> As the main diagnostic tool, we employed magnetic resonance spectroscopy, using both electron spin resonance (ESR) and electron-nuclear double resonance (ENDOR). A number of effects have been observed, some of them still requiring theoretical explanations.

Some of the results of this work were briefly reported in Refs. 5 and 7. Here we present results of ENDOR experiments and more data on the nuclear polarization of the samples. We included an extended description of the previously published work<sup>5,7</sup> along with the details of our apparatus, ending with an overall discussion of the results. The paper is organized as follows: in Sec. II, we present a short review of previous studies carried out on this system with special emphasis on the comparison of different sample preparation methods for attaining the highest H atom concentrations. In Sec. III, we describe in detail our experimental setup together with the diagnostic methods. The experimental results are presented in Sec. IV, followed by discussions and conclusions in Sec. V. Details of the calculations on the dipolar shift and broadening of the electron spin resonance lines are presented in the Appendix.

**II. BACKGROUND**

It has been predicted 40 years ago that light impurities in quantum crystals may behave like an ideal gas, a gas of

impuritons.<sup>2</sup> Generally speaking, a gas of density  $n$  reaches quantum degeneracy when the thermal de Broglie wavelength  $\Lambda_{th}=(2\pi\hbar^2/m^*k_B T)^{1/2}$  exceeds the mean interatomic distance  $\langle r \rangle=n^{-1/3}$ . Atoms that are captured inside solids are not free to move as they can only hop from site to site with a certain probability  $P_h$  which defines the bandwidth of their tunneling motion  $\Delta=ZP_h$  depending on the number  $Z$  of possible sites for tunneling.<sup>8,9</sup> The effective mass  $m^*\sim\hbar^2/a^2\Delta$  of this motion may turn out to be very large, causing the quantum degeneracy temperature to fall far below the experimentally accessible temperature region. Through the study of the quantum diffusion of atoms in solid matrices the tunneling motion band width  $\Delta$  becomes accessible and has therefore motivated experiments in this field. Values of  $\Delta\sim 10^{-4}$  K were extracted from measurements of the diffusion coefficient  $D_{sp}\sim a\Delta^2/\hbar$  of  $^3\text{He}$  in solid  $^4\text{He}$ .<sup>9</sup> It has been found that quantum diffusion is strongly suppressed at high concentrations of impurity atoms. This was explained by the distortion created by the atoms in the lattice. For hydrogen atoms in solid matrices, the main method of measuring the diffusion was to study the recombination of the atoms as they approach each other to within a distance on the order of lattice constant. The diffusion constant  $D_{rec}\sim 10^{-17}$  cm<sup>2</sup> s<sup>-1</sup> obtained in the experiments<sup>10</sup> gives very small values of  $\Delta\sim 10^{-12}$  K. However, just as in the case of mixtures of  $^3\text{He}$  in  $^4\text{He}$ , it has been realized that this type of diffusion is different from the pure diffusion driven by the gradient of atomic density. Instead, as the atoms approach one another, their motion is slowed down due to the energy-level mismatch created by each of them on the neighboring lattice sites thereby slowing down the recombination process.

H atoms moving in the lattice can also induce relaxation of the neighboring ortho-molecules (o-H<sub>2</sub>,  $J=1$ ) to the para state (p-H<sub>2</sub>,  $J=0$ ) and accelerate ortho-para conversion.<sup>11</sup> In this case, there are also restrictions on the H atom movement imposed by the lattice distortions, and so the measured rates do not reflect the spatial diffusion rate of H in H<sub>2</sub>. Neither the measurement of atomic recombination nor the conversion rate can provide information to characterize the pure spatial diffusion.<sup>11-13</sup> To date, there is no experimental data for  $\Delta$  and  $m^*$  for H in H<sub>2</sub>.

The mechanism for the motion of H atoms in solid H<sub>2</sub> was studied in Ref. 14. The studies revealed insensitivity of the recombination rate to applied pressure, suggesting that H atoms move in the H<sub>2</sub> via the chemical exchange reaction  $\text{H}+\text{H}_2\rightarrow\text{H}_2+\text{H}$  instead of physical exchange  $\text{H}_2\leftrightarrow\text{H}$ . The former process has been observed in HD matrices containing atomic impurities.<sup>15</sup> In the case of chemical exchange, the motion of the atom resembles that of a half vacancy, and one might expect a large tunneling probability. It is known that for vacancies in solid helium,  $\Delta$  may be on the order of several kelvins.

It follows from the above discussion that the motion of the stabilized H atoms toward each other and in the vicinity of the lattice defects may be limited at low enough temperatures while still allowing their band motion in undistorted regions of the solid. This would lead to high atom densities in the matrix and open the way to the study of collective quantum phenomena. However, until our recent work (pre-

sented in Refs. 5 and 7) only one study of this system had been carried out at temperatures below 1 K.<sup>16</sup> This work revealed several interesting phenomena which at the time of the experiments were not completely understood. Hydrogen atoms were created by electrons emitted in the  $\beta$  decay of tritium, which was admixed in small amounts into a molecular hydrogen matrix.<sup>16-18</sup> The samples were stored at temperatures ranging from 0.2 to 0.8 K for a period of time until they were destroyed, as indicated by a sudden energy release. This was attributed to a prompt recombination of hydrogen atoms once their density exceeded a critical value, depending on the storage temperature. The sample evolution was analyzed in Ref. 19. Examining the recombination and dissociation processes, the maximum concentration of trapped H atoms in the experiments was estimated to be  $4.6\times 10^{17}$  cm<sup>-3</sup>. It was predicted that concentrations of atoms approaching  $10^{20}$  cm<sup>-3</sup> could be achieved by a proper optimization of the experimental conditions.<sup>19</sup> Nevertheless, no further attempts to reach higher concentrations with this method were reported. For  $T>1$  K, the highest density 270 ppm or  $\approx 7.2\times 10^{18}$  cm<sup>-3</sup> of H in H<sub>2</sub> has been obtained in H<sub>2</sub> doped with 2% of T<sub>2</sub>.<sup>18</sup> However, the T<sub>2</sub> concentration was  $\sim 70$  times larger than the H concentration so that one cannot disregard the effects of T<sub>2</sub> on the sample properties.

Alternative methods used to capture and stabilize H atoms in solid H<sub>2</sub> employed flash condensing a mixture of H and H<sub>2</sub> onto a cold substrate<sup>10,15,20</sup> or direct dissociation of the molecules in the solid through irradiation with  $\gamma$  or  $x$  rays,<sup>13</sup> or high-energy electron beams.<sup>21</sup> However, the maximum density of H in H<sub>2</sub> achieved by these techniques was typically limited to  $\approx 1\times 10^{17}$ – $3\times 10^{18}$  cm<sup>-3</sup>.<sup>10,13</sup>

Another method for creating samples of thin H<sub>2</sub> films containing H atoms below 0.5 K was discovered in our experiments on spin-polarized atomic hydrogen in the gas phase.<sup>5</sup> In these experiments, H atoms are stabilized inside a sample cell (SC) located in a magnetic field of several tesla and at temperatures below 0.5 K. The walls of the sample cell are covered with a film of superfluid helium to reduce adsorption of the atoms on the walls. Recombination of atoms back to molecules, though strongly suppressed in electron and nuclear spin polarized gases, leads to the formation of molecules which eventually adsorb onto the sample cell walls and form a molecular H<sub>2</sub> layer between the sample cell walls and the helium film (see Fig. 1). This layer helps to reduce the rate of nuclear relaxation, improves the stability of the H gas and is usually formed at the beginning of each experiment by sending the maximum available flux of atoms into the sample cell and letting the atoms recombine.<sup>22</sup> In our experiments with two-dimensional (2D) hydrogen gas,<sup>6</sup> we found that H atoms are also captured inside the H<sub>2</sub> films formed by atomic recombination. In that work, the density of atoms adsorbed on the helium surface (Fig. 1) was locally enhanced on a small cold spot on the sample cell walls by the method of thermal compression. Recombination predominantly took place on the high density area of the cold spot via the three-body process  $\text{H}+\text{H}+\text{H}=\text{H}_2^*+\text{H}$ . The third atom carries a rather large kinetic energy, sufficient to penetrate through the helium film and stick to the solid H<sub>2</sub> film.

The main advantage of the method for growing the H in H<sub>2</sub> films by recombination from the gas phase is the very

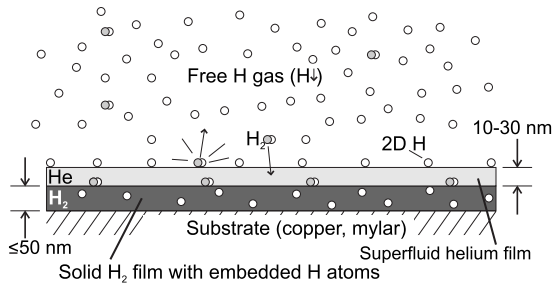


FIG. 1. Illustrative drawing of H in different phases in the SC and the structure of the films covering the SC walls. H adsorbed on the helium surface form a 2D gas, which is in dynamic equilibrium with the bulk gas (Ref. 22). The recombination mainly occurs in the adsorbed phase. The resulting  $H_2$  molecules relax to ground state in collisions with the helium film and finally penetrate through the film (Refs. 23 and 24). Thus a layer of  $H_2$  is grown on the SC walls (Refs. 5 and 6).

small rate of energy release during the sample preparation, enabling low temperature experiments. The samples can be easily further cooled to ultralow temperatures by means of dilution refrigerator and nuclear demagnetizing techniques. The  $H_2$  films are very pure because no other substances, including other H isotopes, can penetrate into the sample cell. However, the samples created in our setup<sup>7</sup> did not exceed H atom densities of  $\sim 10^{18} \text{ cm}^{-3}$  at a typical maximum  $H_2$  film thickness of  $\sim 50 \text{ nm}$ . At such small thicknesses, one must also consider substrate effects. Further disadvantages experienced in this method were the long preparation times, on the order of 1 week, and the need to rebuild the sample completely after each recombination experiment.

Nevertheless, we already found in these first experiments<sup>5</sup> significant differences of the properties of H atoms captured in thin films of  $H_2$  as compared to the experiments performed above 1 K. Below 0.2 K, the samples were completely stable against recombination over 2 weeks observation period and showed an unusual relaxation behavior. The relaxation times of forbidden and allowed electronic transitions were nearly equal and the population of the lowest two hyperfine energy states deviated significantly from the Boltzmann distribution at 150 mK.<sup>5</sup>

In the second stage of our experiments, we tried several methods of forming solid  $H_2$  films from the saturated vapor.<sup>7</sup> We describe these attempts in more detail in Sec. III C. They all failed, and finally we had to use the same method as in Ref. 5, based on the recombination of atoms in the gas phase. In the new sample cell,<sup>7</sup> thermal compression was not used and three-body recombination was no longer the main recombination channel. Even though we were able to create the  $H_2$  films by the same coating procedure, we could not detect H atoms captured in the films. This proves that local three-body recombination in Ref. 5 was a decisive factor for obtaining H in  $H_2$ .

Alternatively, we created atoms in the  $H_2$  films by electron impact.<sup>7</sup> This method has already been employed to dissociate  $H_2$  molecules into atoms in solid  $H_2$ . 160 keV electrons were used in Ref. 21 to create H in  $H_2$  samples at 4 K. In experiments with tritiated hydrogen, 5.7 keV electrons that are emitted from the tritium  $\beta$  decay are already avail-

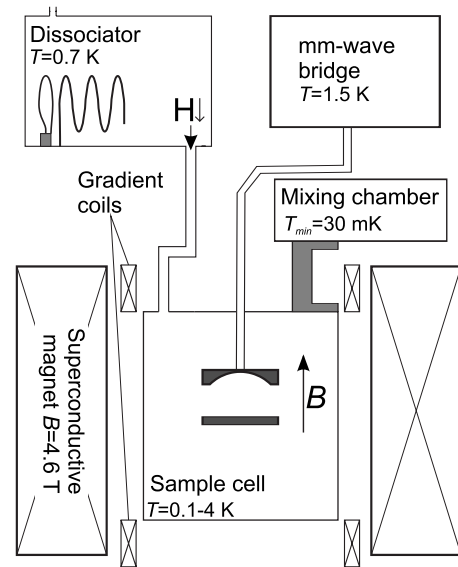


FIG. 2. Block diagram of the experimental setup.

able inside the sample to dissociate hydrogen molecules.<sup>16–18</sup> Low energy electrons are also employed to dissociate hydrogen in a cryogenic dissociator, a device which is routinely used in H gas phase studies including this work.<sup>25,26</sup> The dissociator contains a helical rf resonator located inside a metallic enclosure (see Fig. 2). The inner surfaces of the container and the resonator are covered by a thin layer of  $H_2$  and a superfluid helium film. The discharge is produced by applying rf pulses to the resonator which ionizes helium atoms. The electrons, which are also generated by the discharge, penetrate through the helium film and dissociate  $H_2$  molecules. Some of the atoms created desorb into the gas phase with the others remaining in the solid  $H_2$ . Pulsing the discharge leads to a low average heat release in the sample cell.

In the following section, we provide detailed descriptions of the experimental setup, the procedure for creating the samples of H in  $H_2$ , experimental observations and a comparison of results with those obtained earlier.<sup>5</sup>

### III. EXPERIMENTAL SETUP

#### A. Apparatus

The cryogenic part of the experimental setup is schematically presented in Fig. 2. To fill the SC with hydrogen gas, we use a cryogenic dissociator.<sup>25,26</sup> The dissociator, operating at 0.6–0.8 K, is cooled by a  $^3\text{He}$  refrigerator and is capable of producing a flux of  $H\downarrow \sim 1 \times 10^{14} \text{ s}^{-1}$ . The dissociator is located in the fringing field of a solenoid and atoms in the high-field seeking Zeeman states  $a$  and  $b$  (see Fig. 4) are pulled by the field gradient through the fill line into the SC.

The sample cell is located in the center of a high homogeneity superconducting magnet (4.6 T) and can be cooled down to 70 mK by a dilution refrigerator. The magnet has a set of shim coils reducing the field homogeneity to 0.1 G/cm and a sweep coil capable of producing a  $\pm 400 \text{ G}$  field. In order to realize experiments in large magnetic field gradients,

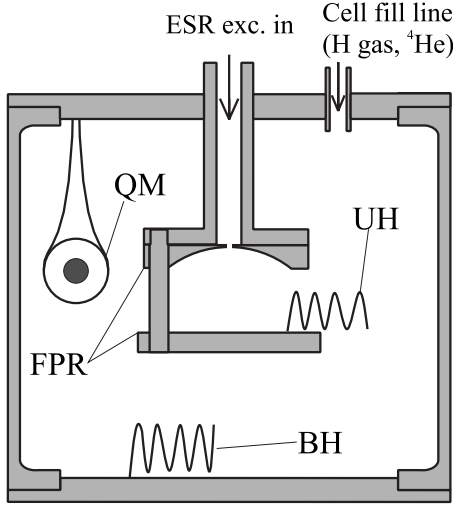


FIG. 3. Schematic drawing of the sample cell. FPR—Fabry-Perot ESR resonator, UH—upper helical rf resonator, BH—bottom helical rf resonator, and QM—quartz microbalance.

we have added a separate gradient coil generating axial gradients up to  $\sim 30$  G/cm.

The main diagnostic tool for studies of atomic hydrogen in our experiments is ESR operating at 128 GHz. The details of this technique will be considered in the next section. The heterodyne cryogenic ESR spectrometer has a sensitivity of  $10^9$  spins/G at an excitation power of several nanowatts.<sup>27</sup> The atoms are detected in a Fabry-Perot resonator (FPR) connected by a waveguide to the millimeter (mm)-wave bridge (Fig. 3).

The SC has two helical rf resonators, both used to run rf discharges for dissociating  $H_2$  in the solid film covering the sample cell surfaces. The lower helix, located on the SC bottom, further referred as bottom helix (BH), has a resonance frequency of 460 MHz and a  $Q$  value of  $\approx 230$ . The second 910 MHz ( $Q \approx 600$ ) helix is located between the FPR mirrors. This helix (upper helix, UH) has a double function. It is tuned to the hyperfine  $a$ - $b$  transition of H to perform both nuclear magnetic resonance (NMR) and ENDOR experiments. The thickness of the  $H_2$  film was measured by a quartz microbalance (QM).

## B. Diagnostic methods

### 1. Continuous-wave ESR

The specific features of our samples are a high degree of electron spin polarization and a high density of the H atoms. These features can lead to dipolar interaction effects and substantial magnetization, both observable in experiments.

Due to the hyperfine interaction, H atoms in the electronic ground state have four energy levels in a magnetic field, labeled from  $a$  to  $d$  with increasing energy. Figure 4 shows the energy states together with the ESR and NMR transitions important in this work. In the 4.6 T magnetic field and at temperatures below 2 K, conditions of the present experiments, the atoms can be considered fully electron spin polarized. The two allowed ESR transitions induced by a trans-

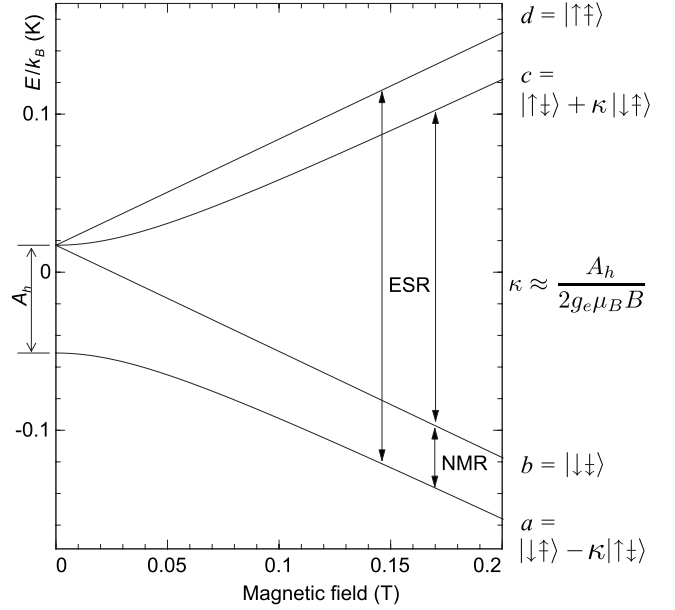


FIG. 4. Ground state H atom energy levels in magnetic field. Here  $\kappa$  is the hyperfine mixing parameter ( $B=4.6$  T,  $\kappa \approx 0.006$ ). Normally the ESR frequency is held constant in these measurements. Arrows denote electron and nuclear spin projections.

verse mm-wave excitation field  $H_1$  are  $a \rightarrow d$  and  $b \rightarrow c$  (Fig. 4). The  $a \rightarrow c$  transition, induced by a longitudinal excitation field, is suppressed by factor  $\kappa^2 \sim 10^{-5}$  at 4.6 T and is therefore strongly forbidden at high magnetic fields. The  $b \rightarrow d$  transition is completely forbidden.

The exact ESR resonance frequencies obtained from the Breit-Rabi equations are

$$f_{bc} = -\frac{1}{2} \frac{A_h}{h} + \frac{1}{2} \frac{\mu^- B_{bc}}{h} + \frac{1}{2} \frac{A_h}{h} \sqrt{1 + \left( \frac{\mu^+ B_{bc}}{A} \right)^2}, \quad (1)$$

$$f_{ad} = \frac{1}{2} \frac{A_h}{h} + \frac{1}{2} \frac{\mu^- B_{ad}}{h} + \frac{1}{2} \frac{A_h}{h} \sqrt{1 + \left( \frac{\mu^+ B_{ad}}{A_h} \right)^2}. \quad (2)$$

Here  $h$  is the Planck constant,  $A_h$  is the hyperfine interaction energy,  $\mu^\pm = g_e \mu_B \pm g_n \mu_n$  where  $g_e$  and  $g_n$  are, respectively, the electron and nuclear  $g$  factors, and  $\mu_B$  and  $\mu_n$  are the Bohr and nuclear magnetons. ESR spectra are detected by a continuous-wave method with a constant mm-wave frequency  $f_0$ , which is normally tuned to the center of the Fabry-Perot resonator curve. Using the sweep coils, the applied magnetic field is swept across the resonance values  $B_{bc}$  and  $B_{ad}$ . The resonant field conditions can be extracted from the equations above setting  $f_{ad} = f_{bc} = f_0$ . In the strong field approximation  $\mu_B B \gg A_h$ , which yields

$$B_{bc} \approx \frac{1}{g_e \mu_B} \left( h f_0 + \frac{1}{2} A_h \right), \quad (3)$$

$$B_{ad} \approx \frac{1}{g_e \mu_B} \left( h f_0 - \frac{1}{2} A_h \right). \quad (4)$$

We find that in the strong field limit, the positions of the ESR lines are mainly determined by the first Zeeman term in the

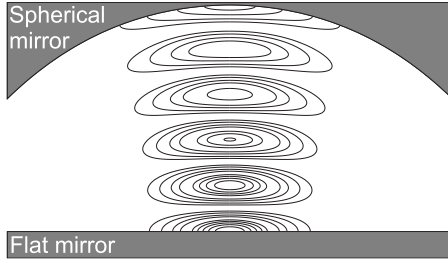


FIG. 5. Contour plot of the mm-wave excitation field  $H_1^2$  in the FPR. The contours are drawn for every 1/10 intensity change.

brackets. The hyperfine interaction determines the splitting between the lines.

Atomic hydrogen is detected in the FPR by the interaction with the mm-wave field. The FPR operates in the  $TEM_{004}$  mode and consists of a lower flat mirror and an upper spherical mirror. The resonator has an aperture of 15 mm and a  $Q$  value of  $\approx 1 \times 10^4$ . The profile of the mm-wave field inside the FPR resonator is shown in Fig. 5. The two FPR resonator mirror surfaces are differently prepared. The upper spherical mirror has a copper surface while the lower flat mirror is covered by a 10  $\mu\text{m}$  Mylar foil glued by a thin layer of Stycast 1266 epoxy in order to realize a smooth surface. The spherical mirror surface was annealed and etched in nitric acid. Presumably it has a much larger surface roughness than that of the flat mirror. Magnetic particles may have collected on its surface due to machining and annealing.<sup>28</sup>

The ESR spectrometer does not use conventional modulation of the magnetic field but instead directly provides absorption and dispersion components of magnetic susceptibility. The strength of the mm-wave field was typically chosen to be below  $10^{-3}$  G, small enough to avoid nonlinear effects. Applying high ESR excitation power at the  $b$ - $c$  transition enabled us to manipulate the populations of the  $a$  and  $b$  states via the forbidden  $a$ - $c$  transition.<sup>5</sup> This effective population transfer of the  $b$  to the  $a$  state is similar to the Overhauser effect used for dynamic nuclear polarization.<sup>29</sup> Typical characteristic time of such a population transfer was  $\sim 300$  s, mainly limited by the available mm-wave power. With this method, we were able to create highly polarized samples with the nuclear spin polarization  $P \equiv (n_a - n_b)/(n_a + n_b) \geq 0.9$ .

In the small excitation regime, the strength of the ESR transitions are proportional to the square of the mm-wave field,  $H_1^2$ . Hence, the recorded line shapes reflect the spatial profiles of the static magnetic field and the mm-wave field inside the samples.<sup>30</sup> An example of the recorded line shape at large axial field gradient is shown in Fig. 8. While the  $H \downarrow$  ESR spectrum reflects the axial profile of the  $H_1^2$  field in the resonator, only two peaks are observed for H in  $H_2$ , one peak for each FPR mirror. Studying the ESR spectra of H in  $H_2$  in a gradient field, we can thus distinguish between the samples on each of the FPR mirrors.

ESR line broadening and shifts of the  $H \downarrow$  gas are very small at densities below  $10^{12}$   $\text{cm}^{-3}$  considered here.<sup>31</sup> Since the  $H \downarrow$  gas spectrum coincides with the spectrum of free atoms, it serves as an ideal reference for the studies of the ESR spectrum resulting from H in  $H_2$  samples. The accuracy

of determining the H in  $H_2$  line shift from the free-atom line is limited by the H in  $H_2$  line broadening (0.7–6 G) and is estimated to be 0.01–0.05 G.

## 2. NMR and ENDOR

The exact and approximate NMR  $a$ - $b$  transition frequencies (Fig. 4) are given by

$$f_{ab} = \frac{1}{2} \frac{A_h}{h} - \frac{1}{2} \frac{\mu^- B}{h} + \frac{1}{2} \frac{A_h}{h} \sqrt{1 + \left( \frac{\mu^+ B}{A_h} \right)^2} \quad (5)$$

$$\approx \frac{1}{2} \frac{A_h}{h} + \frac{g_n \mu_n B}{h}. \quad (6)$$

The hyperfine term  $A_h/2h \approx 710$  MHz is much larger in  $B = 4.6$  T than the Zeeman term  $g_n \mu_n B/h \approx 200$  MHz. Therefore, compared to ESR transitions, the NMR transition is more sensitive to changes of the hyperfine constant  $A_h$  than the ESR transitions. Since on the other hand,  $A_h$  is also sensitive to the lattice crystal field,<sup>32</sup> NMR becomes a very useful tool for studying the environment of H atoms in the solid. The sign of the NMR transition shift with respect to that of the free atoms reflects whether the impurity atoms are located in the substitutional or interstitial lattice sites. In a disordered solid, one would expect a broad NMR line due to a large spread of  $A_h$ .<sup>32</sup> However, in practice NMR has much lower sensitivity than ESR and its direct detection is not possible for the small samples considered in this work. One can overcome the sensitivity problem by detecting the NMR transition via the change in the ESR signal, using the ENDOR method.<sup>33</sup> Saturating the NMR  $a$ - $b$  transition allows manipulation of the  $a$ - and  $b$ -state populations by minimizing the nuclear polarization.

Typically the ENDOR experiment was performed by stopping the sweep field at the  $b$ - $c$  transition. First the complete  $b$ -state atomic population is transferred to the  $a$  state via the forbidden  $a$ - $c$  transition as described above. Then we apply rf power to the upper helix and sweep the frequency through the expected NMR resonance value. When the  $a$ - $b$  resonance is reached, the atoms are transferred back to the  $b$  state and ESR absorption increases. Since the rate of the population transfer back to the  $a$  state is very slow, the signal recorded as a function of the rf frequency represents the total number of atoms transferred from  $a$  to  $b$  since the beginning of the sweep. The actual ENDOR spectrum, i.e., the transition rate as a function of frequency, is reflected by the derivative of the recorded spectrum line shape.

## 3. $H_2$ film thickness and H density measurement

The mean  $H_2$  film thickness covering the SC surfaces is measured by the QM.<sup>34</sup> It was operated at the first harmonic at  $\approx 10$  MHz and had a  $Q$  value of  $5 \times 10^5$ . The QM frequency shifts linearly as a function of the mass adsorbed on it.<sup>35</sup> The QM resonance curve used to obtain its resonance frequency was recorded by measuring the reflected voltage with a network analyzer. The measurement was performed at an incident rf power of  $\leq 0.1$  nW, small enough to avoid any effects due to overheating of the quartz crystal and related

changes in the superfluid film covering its surface. This made possible the measurement of the QM frequency with a short term accuracy on the order of  $\sim 1$  Hz, corresponding to one monolayer solid  $\text{H}_2$ . We estimate the total error of the measured film thickness to be 10%, limited by the slow drifts of the QM during the coating process.

Absolute calibration of the H in  $\text{H}_2$  density requires several steps. First, we calibrate the integrals of the  $\text{H}\downarrow$  gas ESR lines. This is performed calorimetrically, integrating the total heat released in the sample cell during recombination of an  $\text{H}\downarrow$  sample.<sup>6</sup> The ESR signals of  $\text{H}\downarrow$  and H in  $\text{H}_2$  samples are proportional to the product  $n_s \cdot \int_{V_s} H_1^2 dV$ ,<sup>30</sup> where  $n_s$  is the sample density and the integral is taken over the volume  $V_s$  occupied by the sample. The profile of the mm-wave field  $H_1^2$  in the Fabry-Perot resonator is calculated numerically (Fig. 5). Because the H in  $\text{H}_2$  samples are very thin, the  $H_1$  field in the axial direction over the sample thickness  $d$  can be considered constant. Then the integral above can be reduced to  $\sigma_s \cdot \int_A H_1^2 dA$ , where the integration is taken over the area of the mirror and  $\sigma_s$  is the surface density. To determine the bulk density  $n_s$  of H in  $\text{H}_2$ , we divide  $\sigma_s$  by the film thickness obtained from the QM data as described above. We estimate a 20% error in the ESR signal calibration and an overall 30% error for the H in  $\text{H}_2$  density measurement. The dipolar features of ESR spectrum provided another measure for the density in fair agreement with the measurement presented above.

### C. Preparation of the samples

Initial deposition of solid  $\text{H}_2$  films on the walls of the sample cell can be performed by condensing the films from saturated vapor well below the melting pressure. However, in this case the molecules tend to condense at the coldest place on the walls and therefore this procedure requires a careful control of the temperatures of the sample cell. Another difficulty is that liquid  $\text{H}_2$  has different wetting properties for various solids, and tends to collect in form of droplets or puddles,<sup>36</sup> making homogeneous coating impossible. In this work, we did not succeed in producing films by this method.<sup>37</sup> In another attempt, we tried to condense  $\text{H}_2$  using a beam of  $\sim 5$  K molecules blown into the sample cell from a thermally insulated container attached to the SC bottom. Although, relatively thick films were created on the bottom helix, we could not condense any molecules on the mirrors of the FPR resonator, as the high sticking probability of cold molecules to the SC walls inhibits multiple scattering (refer to Fig. 3 for the details of the sample cell geometry). Since no attempt to create a thick homogeneous film of  $\text{H}_2$  by vapor deposition succeeded, we applied the previously successful method described in Ref. 5: slow recombination of the gas phase atoms (see Sec. II). In the second stage,<sup>7</sup> the H atoms trapped inside the  $\text{H}_2$  films were created by electron-impact dissociation of molecules, as described in more detail in the following.

The atoms in the solid  $\text{H}_2$  films were produced by running a discharge in the bottom or the upper helical resonators, in a manner similar to that used for the  $\text{H}_2$  dissociator.<sup>26</sup> Typically, discharges were driven by applying rf power of 10–100 mW in 5–20  $\mu\text{s}$  pulses at a 10–500 Hz repetition rate. We

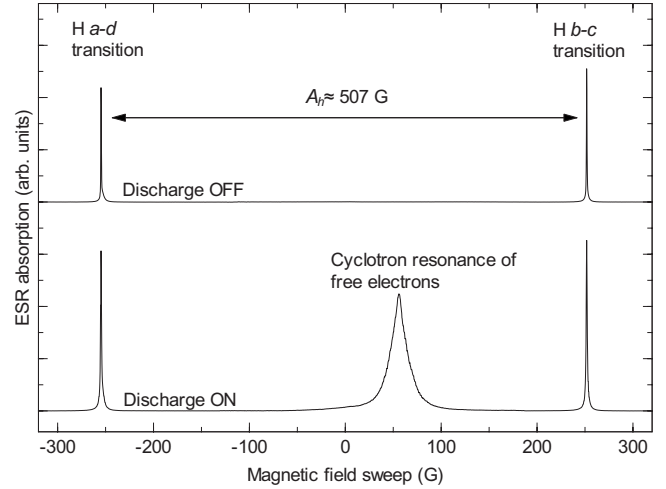


FIG. 6. ESR spectra of atomic H when discharge is off and on. The free-electron ESR transition ( $g_e \approx 2.0023$ ) field is at 0 G on the field sweep axis corresponding to  $\approx 4.6$  T and the cyclotron resonance field is at 53 G.

could maintain the discharge running down to a temperature below 100 mK with an average rf power of several microwatts. The highest density of H atoms in  $\text{H}_2$  was obtained when the SC was heated to 300–400 mK by an average rf power of 40  $\mu\text{W}$ . We estimate the characteristic energy of the electrons emitted in the discharge to be 100 eV. The initiation of the discharge could easily be detected by monitoring the shape of the rf pulse that is reflected from the helix. When running the discharge in the SC we also observed an additional peak in the ESR spectrum, which was attributed to the cyclotron resonance of free electrons (Fig. 6). We observed that the production of atoms was more efficient with the upper helix as electrons produced by the bottom helix must have at least one wall collision before reaching the FPR resonator. Furthermore, H atoms were not only trapped in the  $\text{H}_2$  films but some atoms were also ejected into the bulk of the sample cell in the form of  $\text{H}\downarrow$  gas. The gas phase samples could easily be destroyed by cooling the sample cell to temperatures  $\lesssim 100$  mK. The possibility of accumulating gas phase atoms while running the discharge in the SC implies that the helium film did not evaporate during rf pulses, as otherwise the immediate recombination of  $\text{H}\downarrow$  gas would have resulted.<sup>22</sup>

One expects a high quality  $\text{H}_2$  film due to the ultraslow deposition technique, as supported by our experimental observations<sup>5</sup> and NMR experiments on o- $\text{H}_2$  formed by recombination of atomic H.<sup>38</sup> In this work, the method of subsequently dissociating  $\text{H}_2$  molecules to atoms in the solid by electron impact will create more defects than for single H atoms adhering directly to the  $\text{H}_2$  surface.<sup>5</sup> Charged particles have been observed to be trapped in the  $\text{H}_2$  matrix in methods where molecules are dissociated *in situ* in solid.<sup>21,39,40</sup> In this work, we have not observed any sign of electrons or ions trapped in  $\text{H}_2$ .

The  $\text{H}_2$  films grown by atomic recombination initially contain a large concentration of o- $\text{H}_2$  because it is formed in  $a+b$  recombination. The  $a+a$  recombination leads to p- $\text{H}_2$ .<sup>22</sup> Measuring the steady-state polarization of  $\text{H}\downarrow$  during the

coating we estimate that the initial concentration of o-H<sub>2</sub> in the films does not exceed 30%. Since the natural o-p conversion is continuously going on during the coating we estimated that the H<sub>2</sub> film grown for 1 week by recombination of atoms at constant speed has an o-H<sub>2</sub> concentration of ≈20%, assuming that the molecules are distributed homogeneously through the film by diffusion. The o-p conversion is accelerated by o-H<sub>2</sub> clustering and H impurities.<sup>11,41</sup> Several days after accumulating the sample, the line broadening effect of the remaining o-H<sub>2</sub> in the H in H<sub>2</sub> samples is not observable any more.

Following the accumulation of H in H<sub>2</sub> during the H<sub>2</sub> film growth, we verified that H atoms are uniformly distributed throughout the H<sub>2</sub> film thickness. Typically the H<sub>2</sub> film was grown for coating periods of 30–100 h corresponding to a film growth of 2–10 nm. After each coating period, we accumulated via electron impact a maximum density of H at the optimal conditions. The linear increase in the maximum H in H<sub>2</sub> ESR line areas with the film thickness implies the same H density and consequently a uniform distribution in the H<sub>2</sub> film.

#### IV. RESULTS

In this section, we present experimental results of a single experimental run with a H<sub>2</sub> film of 30 nm thickness. In order to allow a comparison to our previous work,<sup>5</sup> we first accumulated a H in H<sub>2</sub> sample of similar density  $2 \times 10^{18}$  cm<sup>-3</sup> by running the discharge in the bottom helix. The subsequent samples were prepared by running the discharge in the upper helix and had initial densities of  $2 \times 10^{19}$  cm<sup>-3</sup>. Each of the H in H<sub>2</sub> samples was typically studied for 1–2 weeks. By the end of these studies, the H atom density had decreased at least by a factor of 2 due to recombination studies performed at higher temperatures (0.5–1.7 K). Because the properties of the samples accumulated by the bottom and upper helices differed, we will hereafter refer them, respectively, as bottom helix and upper helix samples.

##### A. ESR spectrum

###### 1. Characteristic features of the ESR spectrum of H in H<sub>2</sub>

The ESR spectrum of H<sub>↓</sub> gas is presented in Fig. 6 (upper trace). The two lines correspond to the  $a \rightarrow d$  ( $a$ -line) and  $b \rightarrow c$  ( $b$ -line) transitions, separated by  $A_h/g_e\mu_B \approx 507$  G. In the lower trace, the ESR spectrum recorded during continuous operation of the rf discharge is shown. The additional peak in the center appears due to the cyclotron resonance of free electrons generated by the discharge.

Typical ESR spectra of low and high density H in H<sub>2</sub> samples are compared to the H<sub>↓</sub> gas sample in Fig. 7. The H<sub>↓</sub> ESR lines are inhomogeneously broadened to ≈50 mG full width at half maximum (FWHM) at optimized homogeneity of the magnetic field. The H in H<sub>2</sub> ESR lines are much broader and shifted from the H<sub>↓</sub> lines. The shifts and widths of the H in H<sub>2</sub> lines are density dependent. The H in H<sub>2</sub> lines move to positive magnetic fields when the H atom density is increased.

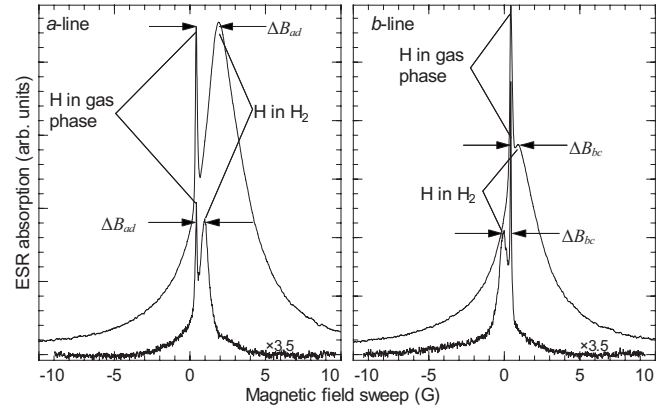


FIG. 7. ESR spectra of atomic hydrogen in the gas phase and in the solid H<sub>2</sub> matrix in magnetic field of optimized homogeneity. The upper traces were recorded at the H in H<sub>2</sub> density of  $n \approx 2 \times 10^{19}$  cm<sup>-3</sup>, the lower traces were recorded at  $n \approx 6 \times 10^{17}$  cm<sup>-3</sup> and multiplied by the factor 3.5 compared to the high density traces. The  $\Delta B_{ad}$  and  $\Delta B_{bc}$  indicate the shift of the H in H<sub>2</sub> line from the H<sub>↓</sub> line for  $a$  and  $b$  lines, respectively.

In a strong axial magnetic field gradient, each line splits into two peaks (Fig. 8 top) originating from contributions of the flat and spherical mirrors, respectively. The axial gradient does not distort the intrinsic line shape because the samples are thin in the axial direction and the spherical mirror curvature is small. Both peaks are fitted well by Lorentzian functions. Their areas reflect the density and nuclear polarization of each mirror sample. A comparison of the areas shows that the H in H<sub>2</sub> densities on each mirror was equal to within 10%, implying an even distribution of H on the FPR surfaces. However, the shifts between the H in H<sub>2</sub> lines and the H<sub>↓</sub> line cannot be found accurately in an axial gradient because the H<sub>↓</sub> line is strongly broadened (Fig. 8 bottom). Therefore the shifts  $\Delta B_{ad}$  and  $\Delta B_{bc}$  were measured in the field of maximum homogeneity (Fig. 7).

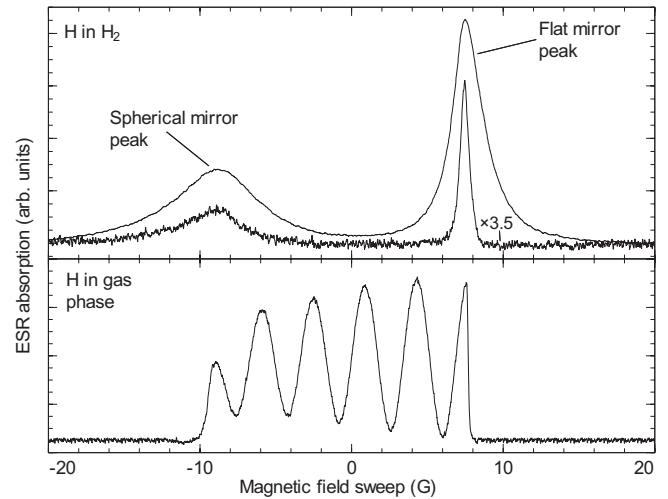


FIG. 8. ESR  $a$ - $d$  transition spectra of H in H<sub>2</sub> and H<sub>↓</sub> gas at an axial magnetic field gradient of 25 G/cm. The H<sub>↓</sub> spectrum in the lower panel reflects the axial profile of the mm-wave  $H_1^2$  field in the resonator (Fig. 5). The upper H in H<sub>2</sub> spectrum was recorded at  $n \approx 2 \times 10^{19}$  cm<sup>-3</sup> and the lower (multiplied by the factor 3.5) at  $n \approx 6 \times 10^{17}$  cm<sup>-3</sup>.

The ESR linewidth for the sample on the spherical mirror was found to be  $\approx 6$  G, independent of the H density. In contrast, the line widths for the sample on the flat mirror were found to be proportional to the density. Studying electron spin relaxation behavior of the samples on the flat and spherical mirrors, we found that the ESR line of the former is homogeneously broadened while the sample on the spherical mirror was inhomogeneously broadened.

A probable reason for these differences is the different substrates. The spherical mirror surface is polycrystalline copper and has more roughnesses than the flat mirror. It may contain small concentrations of ferromagnetic impurities,<sup>28</sup> which may facilitate fast relaxation and lead to the inhomogeneous broadening. The Mylar surface is known to be very smooth and homogeneous, with weak van der Waals attraction to the adsorbed atoms. Therefore, the flat mirror sample relaxation and ESR line broadening is determined only by the interactions of the H atoms with the host matrix and with each other, as will be discussed in more detail in the following sections. The samples on the flat and spherical mirrors will hereafter be referred to as copper and Mylar substrate samples, respectively.

**2. Dipolar broadening and shifts of the ESR lines**

The linewidths of the H in H<sub>2</sub> spectra observed in this work were much broader than those observed in our earlier experiments.<sup>5</sup> The width of the Mylar substrate sample line was found to depend on the atomic density and on the history of the sample (Fig. 9). To explain these observations, we consider two main sources of broadening: Dipolar interaction between magnetic dipoles and constant broadening due to other sources. The dipolar broadening of magnetic resonance lines is caused by the spread of the local magnetic field experienced by atoms randomly positioned in the lattice. For atoms with identical spin states, the dipolar interaction and the concomitant broadening is enhanced by a factor of 3/2 due to the coherent interaction of oscillating dipoles.<sup>42,43</sup>

Broadening due to dipolar interaction with o-H<sub>2</sub> has been observed in the experiments of the Nagoya and Moscow groups<sup>13,44</sup> as well as in our earlier work.<sup>5</sup> In the case of o-H<sub>2</sub>, broadening the ESR linewidth depends on the o-H<sub>2</sub> concentration and may vary between 0.2 and 1 G. In the present work, the influence of o-H<sub>2</sub> was observed by the narrowing of the ESR lines during the first days after creation of a low density sample in a new H<sub>2</sub> film [Fig. 9(b)]. As estimated above, we may have a maximum initial concentration of o-H<sub>2</sub> of  $\sim 20\%$ , which slowly decreases in time due to the natural and stimulated conversion processes.<sup>11,41</sup> Line broadening at higher densities and its linear dependence on the H concentration can be explained by the dipole-dipole interaction between hydrogen atoms.

We observed the broadening due to atoms in the like and unlike spin states<sup>42,43</sup> by recording the *a* and *b* line as a function of polarization (Fig. 10). At high nuclear polarization  $P \approx 0.8$  most of the atoms are in the *a* state, and the *a* linewidth is influenced by the interactions with identical atoms. In contrast, the *b* linewidth is broadened mainly by unlike *a* atoms, and its width is  $\approx 3/2$  times smaller than the *a* linewidth. When the sample relaxes back to nearly equal

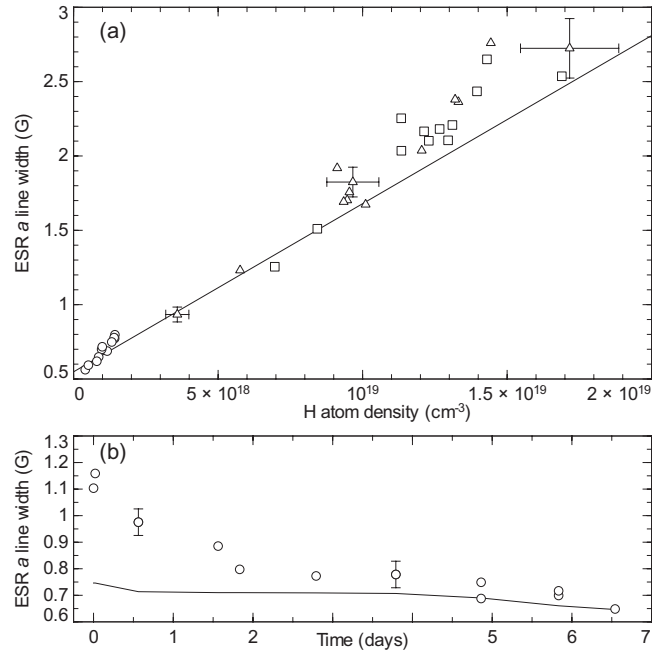


FIG. 9. H in H<sub>2</sub> ESR line broadening. (a) Full width at half maximum of ESR *a*-line Mylar substrate sample line as a function of total density  $n = n_a + n_b$ . Different symbols are used for different samples: (○) bottom helix sample, (△, □) upper helix samples. (b) Line narrowing of bottom helix sample during sample storage at  $< 0.2$  K ( $n \approx 1 \times 10^{18}$  cm<sup>-3</sup>). The solid lines in (a) and (b) are results of the ESR line shape simulation neglecting the o-H<sub>2</sub> contribution. The measurements were performed at  $n_a/n_b \sim 2$ .

populations of hyperfine states ( $P=0$ ), the widths of the lines approach each other.

To account for the density-dependent shifts of H in H<sub>2</sub> lines, we consider the effects of a change in the hyperfine interaction constant  $\Delta A_n$  and the magnetization  $\Delta B_{dip}$  of the sample. In the latter case, the internal dipolar field  $\Delta B_{dip}$  is dependent on the density and the shape of the sample, and is directed for thin enough films opposite to the static polarizing field (see Appendix). To compensate for the resulting

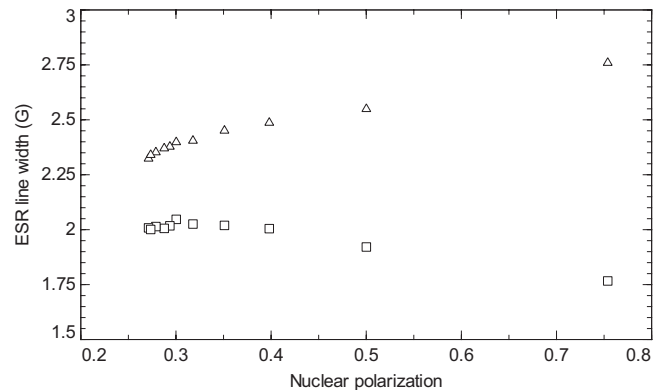


FIG. 10. Difference in the ESR line broadening due to the interactions between like and unlike atoms. The widths of the *a* (△) and *b* (□) ESR lines of the Mylar substrate sample (created by upper coil) are shown as a function of nuclear polarization  $P$ .  $P = (n_a - n_b)/(n_a + n_b)$ ,  $T = 120$  mK, and  $n = 1.5 \times 10^{19}$  cm<sup>-3</sup>.

reduced field experienced by atoms, we have to apply larger sweep fields so that the lines appear to be shifted toward higher magnetic fields. This effect has been observed previously in paramagnetic substances<sup>45</sup> and in experiments with 2D gases of electron spin polarized H atoms adsorbed on helium surfaces.<sup>6,46</sup> A modification of the electron  $g$ -factor  $g_e$  by the solid matrix can also cause the line shift.<sup>20,32</sup> However, this effect is independent of the H density and contributes a constant term in the magnetization. So far the  $g$  factor change has been found to be negligible for H atoms in H<sub>2</sub>.<sup>5,20</sup>

Using Eqs. (3) and (4) describing the approximate resonance fields of a free atom and H in H<sub>2</sub>, we obtain the ESR line shifts for the  $a$ - $d$  and  $b$ - $c$  transitions,

$$\Delta B_{ad} = -\frac{1}{2} \frac{\Delta A_h}{g_e \mu_B} - \Delta B_{dip}, \quad (7)$$

$$\Delta B_{bc} = \frac{1}{2} \frac{\Delta A_h}{g_e \mu_B} - \Delta B_{dip}. \quad (8)$$

The change in the hyperfine constant  $\Delta A_h$  shifts the  $a$ - $d$  and  $b$ - $c$  ESR lines in opposite directions while the magnetization change  $\Delta B_{dip}$  has the same effect on both of them. Using the above equations, the changes of the hyperfine constant and of the magnetization are

$$\Delta A_h = g_e \mu_B (\Delta B_{bc} - \Delta B_{ad}), \quad (9)$$

$$\Delta B_{dip} = -\frac{\Delta B_{bc} + \Delta B_{ad}}{2}. \quad (10)$$

Here we neglected the effect of like spins, as due to the small nuclear polarization during the measurements the shifts for both ESR lines are similar. However, in the further analysis of the dipolar interaction effects, the like spin effect is included.

In our experiments, we find that  $\Delta A_h$  is different for the samples created by the bottom and upper helices. For the low density sample created by the bottom helix  $\Delta A_h = -1.7(5)$  MHz whereas for the high density upper helix sample,  $\Delta A_h = -3.5(6)$  MHz. More accurate measurements of the  $\Delta A_h$  are performed using the method of double resonance introduced in the next section. The extracted magnetization  $-\Delta B_{dip}$  as a function of H concentration is presented in Fig. 11 together with the result of a computational-statistical simulation described below.

A common method of characterizing dipolar broadening of magnetic resonance lines in crystals is the method of moments.<sup>42,43</sup> However, when the line shape is non-Gaussian, the analysis is less straightforward.<sup>43,47</sup> In our case, the electron spin polarization, sample shape, and experimental spectrum under gradient lead to further complications.

In this work, we employed a computational-statistical method for direct calculation of the line shapes in the local field approximation.<sup>48,49</sup> The method allows us to take into account the important features of our experimental system. The distribution or histogram of local dipolar fields experienced by an atom is computed directly by first placing the atoms in the lattice randomly and then adding together their

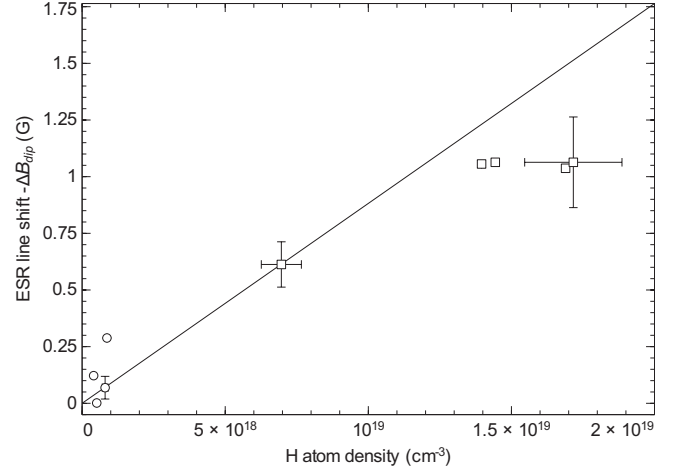


FIG. 11. Density-dependent shift of the ESR lines. Different symbols are used for different samples: (○) bottom helix sample and (□) upper helix sample. The solid line represents the result of simulation described in the Appendix. The measurements were performed at  $n_a/n_b \sim 2$ .

dipolar fields. The shape of the local field histogram reflects the line shape due to dipolar interactions.<sup>47,49</sup> The details of the line shape simulations are described in the Appendix.

The calculations for the broadening and line shift are plotted as solid lines in Figs. 9 and 11. The simulations agree well with the experiments and present a verification of the film thickness measurement and ESR density determination.

## B. ENDOR spectra and hyperfine interaction changes

ENDOR spectra were recorded for the samples created by the upper and bottom helices and at different stages of the sample history. A typical ENDOR spectrum recorded at low ESR excitation power is presented in Fig. 12. Preceding the NMR frequency sweep the entire population of the  $b$  state was driven into the  $a$  state via the forbidden  $a$ - $c$  transition so that the ESR absorption for the  $b$  line was close to zero. Applying the rf power to the upper helix and sweeping its frequency (starting from the right in Fig. 12), we observed two narrow ( $\leq 20$  kHz) lines. The first line was shifted by  $\approx 660$  kHz and the second line shifted by 1560 kHz from the free-atom frequency  $f_{ab}^0$  toward lower frequencies (Fig. 12). The first line was more intense for the low density samples created by the bottom helix whereas the second line was a strong characteristic feature for the high density samples created by the upper helix. The upper helix sample spectrum also features a weak wing extending 400 kHz toward the free-atom frequency. We were able to extract the relative number of spins belonging to each transition by comparing the change in the ENDOR signal to the maximum possible increase in the  $b$ - $c$  transition intensity near saturation, when the  $a$ - and  $b$ -state populations were almost equal. Reducing the density of the upper helix sample by recombination, we observed that the first ENDOR line disappeared completely while the area of the second line relative to the wing did not change. For the sample created by the upper helix, we found that 80% of the atoms occupy the second line, 15% the wing

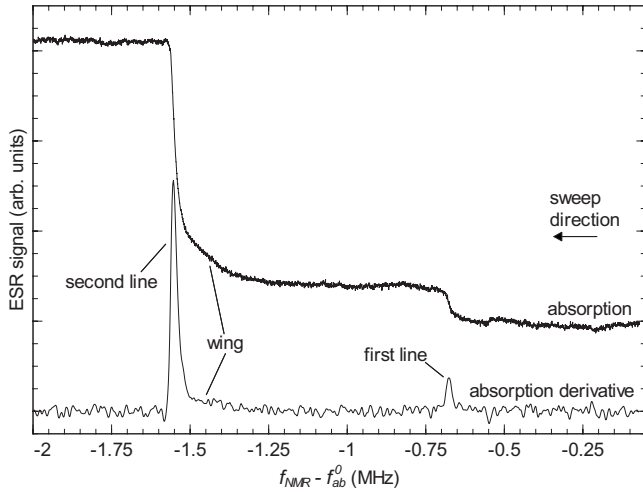


FIG. 12. ENDOR spectra of Mylar substrate sample accumulated by the upper helix. When the NMR transition is induced, the  $b$ -state population increases and hence the ESR  $b$ - $c$  transition absorption increases.  $f_{ab}^0$  is the free H atom resonance frequency. The lower trace is the derivative spectrum. Note the sweep direction from right to left.

and the remaining 5% the first line. In the bottom helix sample, more than 50% of atoms were associated with the first transition.

The hyperfine constant changes for the first and the second line,  $\Delta A_{h1} = -1320(10)$  kHz and  $\Delta A_{h2} = -3070(10)$  kHz, are in agreement with the results of the ESR measurements presented in the previous section. The position of the first transition coincides with the one reported in our previous work.<sup>5</sup> The shift of the hyperfine constant for the second line  $\Delta A_{h2}$  is  $\sim 200$  kHz smaller than the value obtained in Ref. 20 in measurements which were performed in the K-band ESR on flash condensed H in  $H_2$  samples at 4 K.

The narrow ENDOR transitions indicate that a majority of the atoms (60–80%) are located in areas of homogeneous crystalline field of the host  $H_2$  crystal. The negative sign of the hyperfine interaction change implies that the atoms are located in substitutional sites in the host lattice.<sup>20,32</sup> A similar conclusion was derived in distant ENDOR experiments,<sup>50</sup> which differ from the method presented here. It is based on the interaction of the  $o$ - $H_2$  nuclear spin system and the H electron spin system and gives information on the  $o$ - $H_2$  molecules surrounding the H atoms.<sup>33</sup> The appearance of two ENDOR lines, possibly caused by the existence of two different available lattice sites for the atoms, will be considered in the discussion section.

### C. Recombination

Recombination of H atoms in  $H_2$  crystals is a two-body process, described by the second order kinetic equation,

$$\frac{dn}{dt} = -2K_r n^2, \quad (11)$$

where  $K_r$  is the recombination rate constant and  $n = n_a + n_b$  is the total H atom density. Consequently, the inverse density

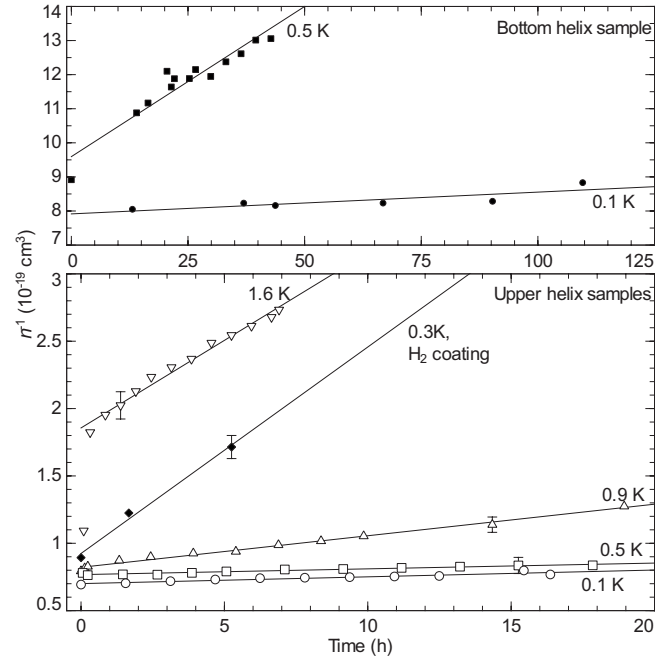


FIG. 13. Recombination measurements of Mylar substrate samples at different temperatures. Upper graph: bottom helix sample and lower graph: upper helix samples. For the recombination measurement during  $H_2$  coating ( $\blacklozenge$ ), only the first points are presented here since the recombination rate was observed to slow down at lower density.

$n^{-1}$  has a linear dependence on time with the slope  $2K_r$ . Electronic polarization of the atoms was found to have no effect on the recombination rate.<sup>5,10</sup> In the present experiments also nuclear polarization<sup>10</sup> had no effect on the recombination rates. In Fig. 13, the inverse density  $n^{-1}$  is plotted as a function of time for the recombination measurements with the Mylar substrate samples at temperatures between 0.1 and 1.6 K. The corresponding rate constants determined by the slope are presented in Fig. 14 as a function of temperature.

We neither observed any difference in the recombination rates between the Mylar and copper substrate samples nor any effects of the sample aging. In all measurements, the inverse density was found to be a linear function of time, in agreement with Eq. (11). However, as can be seen in Fig. 14, the low density sample created by the bottom helix decayed much faster at 0.5 K than the high density ones created by the upper helix. This difference in the decay rate might be explained by the different concentration of defects in the samples. Warming up the upper helix sample to 1.6 K decreased the density by a factor of 2 within the first  $\sim 5$  min of the measurement. This is somewhat similar to the observations in Refs. 16 and 52 but because in our case the very small sample is distributed over a large surface area, a fast recombination did not lead to a thermal explosion. Heating the SC further to 2 K resulted in a decrease in the  $H_2$  film thickness and limited the highest achievable temperatures of the recombination studies.

We measured the H density in the  $H_2$  films during the process of  $H_2$  coating by recombination of  $H\downarrow$  at  $T \approx 0.3$  K (Fig. 13) and observed a much faster density decrease than without the coating. Before the measurement, we had built

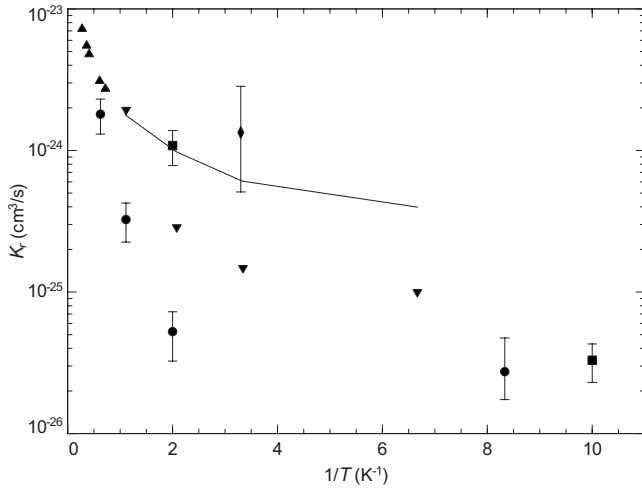


FIG. 14. Recombination rate constants of the Mylar substrate sample created by the bottom and upper helices. Present work:  $\blacksquare$ —low density bottom helix sample,  $\bullet$ —high density upper helix sample,  $\blacklozenge$ —high density upper helix sample under  $\text{H}_2$  coating. Previous experiments:  $\blacktriangledown$ — $T < 1$  K (Ref. 5),  $\blacktriangle$ — $T > 1$  K (Ref. 51). Theoretical prediction—line (Ref. 8). The  $\text{H}_2$  coating point ( $\blacklozenge$ ) error bars contain the decrease in the recombination rate at smaller density.

an  $\text{H}_2$  film and accumulated H atoms in it by running a discharge in the upper helix. Since the film thickness during the first 5 h of coating grew only by  $\lesssim 5\%$ , it cannot account for the observed density decrease. Instead, the recombination enhancement during the process of  $\text{H}_2$  coating can be explained by the strong flux of phonons resulting from the  $\text{H}\downarrow$  recombination which propagated into the solid matrix. In irregular crystals, the phonons support the process of atoms hopping from one lattice site to another and approaching each other to catalyze recombination.<sup>8</sup> This process could also have been responsible for reaching relatively low H densities in our previous work<sup>5</sup> and explains the stability of the samples observed in our work<sup>5,7</sup> at temperatures below 1 K. The lack of excitations in the lattice did not permit atoms to approach and recombine.

#### D. Nuclear relaxation

For a nondegenerate atomic system, the populations of the hyperfine states  $a$  and  $b$  in thermal equilibrium are related via the Boltzmann factor  $n_a/n_b = \exp(E_{ab}/k_B T)$ , where  $E_{ab} \approx 48$  mK is the energy difference between the states for a magnetic field of 4.6 T. In our previous work, we observed significant deviations from this law at a temperature of  $\approx 150$  mK.<sup>5</sup> In the current work, we performed detailed studies of the steady-state nuclear polarization  $P = (n_a - n_b)/(n_a + n_b)$  as a function of temperature. This has been done by driving the system out of thermal equilibrium and then following its relaxation. Nonthermal hyperfine level populations were created by saturating the  $a$ - $b$  transition using the upper helix ( $P \rightarrow 0$ ) leading to an excess of  $b$  atoms with respect to the Boltzmann factor, or by saturating the  $b$ - $c$  transition with subsequent transfer of the  $b$ -state atoms into the  $a$  state via the forbidden  $a$ - $c$  transition ( $n_a \gg n_b$ ,  $P \rightarrow 1$ ).

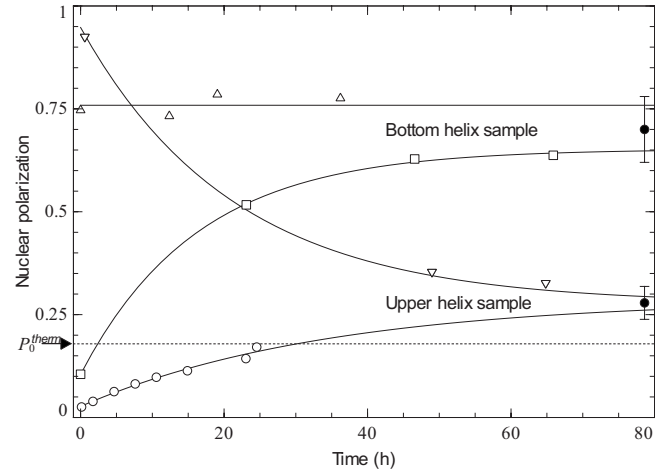


FIG. 15. Nuclear relaxation experiments of Mylar substrate samples created by discharge in bottom helix and in upper helix at 120 mK. ( $\Delta$ ,  $\square$ )—bottom helix sample of  $n_H \approx 2 \times 10^{18} \text{ cm}^{-3}$ , ( $\nabla$ ,  $\circ$ )—upper helix sample of  $n_H \approx 1.5 \times 10^{19} \text{ cm}^{-3}$ , and  $\bullet$ —the extracted steady-state polarizations. The thermal polarization  $P_0^{\text{therm}} \approx 0.18$  is indicated by the dashed line. The solid lines are fits to the experimental data. The initial polarization in ( $\Delta$ ) turned out to be close to  $P_0$  and no relaxation was observed.

Typical relaxation measurements of the Mylar substrate sample created by the bottom and upper helices are presented in Fig. 15. The steady-state polarization  $P_0$  and nuclear spin-lattice relaxation time  $T_n$  were extracted by fitting the experimental data with the equation,

$$P(t) = P_0 + A e^{-t/T_n}, \quad (12)$$

where  $A$  is a free fit parameter depending on the initial deviation of the polarization from equilibrium.

In Fig. 16, we present a summary of the measured steady-

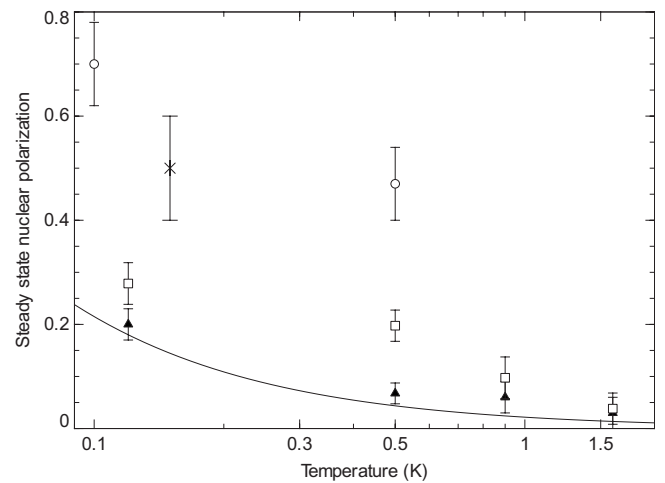


FIG. 16. Steady-state polarizations of different samples at different temperatures.  $\circ$ —low density Mylar substrate sample created by bottom helix,  $\square$ —high density Mylar substrate samples created by upper helix,  $\blacktriangle$ —copper substrate samples created by upper helix, and  $\times$ —earlier work (Ref. 5). The solid line corresponds to the Boltzmann distribution.

state polarizations for the samples on both mirrors created by the bottom and upper helices. While the copper substrate sample relaxes to a Boltzmann distribution, the steady-state nuclear polarization  $P_0$  of the Mylar substrate samples deviates from a Boltzmann distribution. The deviation becomes larger for the low density sample created by the bottom helix, in fair agreement with our previous work.<sup>5</sup> We did not observe a dependence of  $P_0$  on the sample storage time, in contrast to the nuclear relaxation time which slowed down considerably during 2 weeks of observations. However, the change in  $T_n$  turned out to be small enough in a single relaxation measurement to consider it as a constant in the fitting procedure. The copper substrate sample  $T_n$  was found to be an order of magnitude smaller ( $T_n \sim 1$  h) than that of the Mylar substrate sample. This is not surprising since the interaction of the atoms with the copper substrate is much stronger than with the Mylar substrate. The same effect seems to be responsible for the inhomogeneous broadening of the ESR lines in the copper substrate sample (see Sec. IV A).

## V. DISCUSSION AND CONCLUSIONS

We reached  $2 \times 10^{19} \text{ cm}^{-3}$  (0.1%) densities of H in  $\text{H}_2$ , three times larger than ever observed in this system, and 20 times larger than in our previous work.<sup>5</sup> This has been achieved with a new method of dissociating the  $\text{H}_2$  molecules *in situ* in the solid films by bombarding them with electrons resulting from an rf discharge operating below 0.5 K. The samples showed higher stability against the recombination of H atoms compared to previous experiments which were performed at temperatures above 1 K and with samples created by different methods. The stability enhancement can be explained by the lack of excitations, which would enable the movement of atoms toward each other and recombination at higher temperatures.<sup>5,8</sup> Better stability of the high density samples compared to the low density samples can be explained by the reduced mobility of H atoms trapped by the lattice distortions. Those can result from vacancies or dislocations created during the sample preparation or from the H atoms themselves. Our experiments provide strong support for the latter. Injecting an extra flux of phonons into the lattice significantly accelerated the recombination rate of H atoms.

These observations point the way for producing even higher concentrations of H in  $\text{H}_2$  crystals by further reducing the heat release in the solid matrix during the sample preparation. We suggest implementing a method of cold molecular and atomic beam epitaxy to grow the H in  $\text{H}_2$  films. Cold ( $< 0.5$  K) beams of H atoms are readily available in laboratories studying  $\text{H}\downarrow$  gas.<sup>6</sup> Molecular  $\text{H}_2$  beams with temperatures on the order of few kelvins can be obtained by sublimation from the solid phase. Directing these beams simultaneously onto a cold ( $T < 0.5$  K) substrate would allow growth of samples with a maximum heat release on the order of 4.6 eV, generated in the occasional recombination of atoms. This is substantially lower than  $\geq 6$  eV released in each dissociation event in the current method or what is achieved by currently used sample preparation methods.

We observed a strong influence of the substrate on the properties of the H in  $\text{H}_2$  films. For the samples deposited on a high-purity polycrystalline copper surface, we found that the ESR lines are inhomogeneously broadened. On the contrary, for samples located on the surface of the Mylar film we recorded homogeneously broadened lines and approximately ten times longer nuclear relaxation times. We explain this difference by the inhomogeneities of the crystalline field due to the polycrystalline structure of copper or possible magnetic impurities embedded in its surface.

The broadening of the ESR lines of the Mylar substrate sample was explained by the dipolar interactions of the H atoms with surrounding ortho- $\text{H}_2$  molecules and with each other. The latter effect dominates at high densities. In this case, the ESR linewidth is proportional to the H atom concentration and depends on the nuclear polarization of the sample. We observed the difference by a factor of 3/2 in the line broadening caused by the dipolar interaction between like and unlike spin states.<sup>42,43</sup> In addition, we observed a density dependent shift of the ESR lines from the positions of the free-atom transitions. The shifts can be interpreted in terms of an internal dipolar field or macroscopic magnetization. These explanations are supported by numerical models performed on the line shapes and shifts, which coincide well with the experimental observations.

Studying the effect of the host matrix on the impurity H atoms by means of ENDOR revealed two sharp transitions shifted to the red from the free-atom transition. This indicates two possible H atom occupation sites in the  $\text{H}_2$  lattice. The negative sign of the transition shift implies that the atoms are located in substitutional positions. For the atoms in the interstitial sites, on the contrary, the hyperfine interaction is enhanced.<sup>32</sup> The first transition found in our work (due to the first kind of atoms), corresponding to a change in the hyperfine constant of  $\Delta A_h \approx -1.3$  MHz, was observed mainly for low H atom density samples ( $n_H \lesssim 3 \times 10^{18} \text{ cm}^{-3}$ ). The second much stronger transition at  $\Delta A_h \approx -3.1$  MHz was observed for the samples with higher H atom densities. Studying the recombination of H atoms, we found that the first kind of atoms recombines faster than the second kind, indicating their higher mobility. This might be understood in terms of a stronger coupling of the second kind of atoms to the lattice, which are possibly trapped near vacancies or dislocations of the lattice. The stronger delocalization of the H electron in the vicinity of a vacancy should lead to a larger reduction in the hyperfine constant, in agreement with the observations for the atoms of this kind. However, the small width of the observed ENDOR transitions implies a homogeneous crystalline field experienced by the atoms and does not support the suggestion above. Further work is required to resolve this problem.

The most intriguing observation of our previous and current work is the significant deviation of the steady-state nuclear polarization from the value determined by the Boltzmann statistics. The deviation was substantially larger for the lower density samples on the Mylar substrate, containing mainly the first kind of atoms. Since the population of the lower energy (ground) state is enhanced, we suggested in our previous work that this phenomenon can be related to Bose-Einstein condensation (BEC) of the impurity atoms. How-

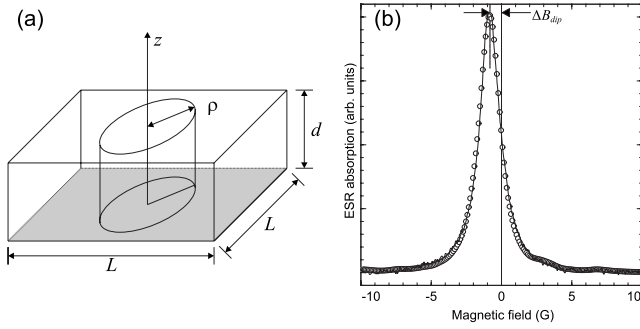


FIG. 17. (a) Schematic drawing of the simulation object. Local fields are calculated for atoms which are located within a distance  $\leq \rho$  from the  $z$  axis. (b) Comparison of experimental (continuous line) and simulated (circles) line shapes,  $n = 1 \times 10^{19} \text{ cm}^{-3}$  and  $n_a/n_b \approx 2$ . The simulation parameters are:  $L = 500 \text{ nm}$ ,  $d = \rho = 30 \text{ nm}$ , and the histogram was computed with 100 points/G but reduced to 10 points/G in the plot.

ever, the average densities obtained so far are not enough to reach BEC at the temperatures of the experiment, even assuming that the effective mass of the impurity atoms is close to the H bare mass. The deviation from Boltzmann behavior seems to increase gradually when the temperature is lowered (Fig. 16) and does not allow a determination of the critical temperature. This is reasonable considering that BEC is a second or third order transition. On the other hand, the samples deposited on the curved mirror corresponding to a copper substrate do not appear to deviate from the Boltzmann distribution (see Fig. 16). Further studies of this system will be needed to understand this complex phenomenon.

#### ACKNOWLEDGMENTS

This work was supported by the Academy of Finland (Grants No. 122595 and No. 124998), the Wihuri Foundation, and NSF under Grant No. DMR 0504683. J.A. thanks the NGS-NANO, J.J. and O.V. thank the Finnish Cultural Foundation. We thank K.-A. Suominen, R. Laiho, and S. Jaakkola for support and E. Mueller and N. Ashcroft for helpful discussions.

#### APPENDIX: DIPOLAR INTERACTION EFFECTS IN THE ESR SPECTRA

The experimental line shape was modeled by calculating the probability distribution of the local dipolar fields of H atoms in the  $\text{H}_2$  film. The local fields were obtained for random distributions of atoms in a model lattice. The lattice is a square slab resembling the geometry of the  $\text{H}_2$  film, with thickness  $d$  and lateral dimension  $L_x = L_y \equiv L$ ,  $L \gg d$  [Fig. 17(a)]. The fields are calculated for atoms which are located inside a cylinder of radius  $\rho \ll L/2$ , centered on the  $z$  axis. This allows the average magnetization near the upper and lower film surfaces to be taken into account. The maximum volume of the model film  $L^2 d$  and thus the number of H atoms  $nL^2 d$  was limited by the computational time so not more than  $10^6$  dipoles were used in the calculations.

The local field experienced by an atom in the model film was obtained by summing the dipolar fields created by the remaining dipoles. At location  $\mathbf{r}_j$ , the magnetic field induced by a single dipole located at  $\mathbf{r}_i$  is given by

$$\mathbf{B}_d(\mathbf{r}_{ij}) = \frac{\mu_0}{4\pi} \frac{3(\mathbf{m} \cdot \mathbf{r}_{ij})\mathbf{r}_{ij} - \mathbf{m}|\mathbf{r}_{ij}|^2}{|\mathbf{r}_{ij}|^5}, \quad (\text{A1})$$

where  $\mathbf{m} = g_e \mu_B \hat{\mathbf{e}}_i / 2$  is the magnetic moment of the dipole at  $\mathbf{r}_i$  ( $\hat{\mathbf{e}}_i \parallel \mathbf{B}_0$ ) and  $\mathbf{r}_{ij} = \mathbf{r}_j - \mathbf{r}_i$ . The enhancement of the dipolar interaction between like atoms can be taken into account by an additional factor  $3/2$  in Eq. (A1).<sup>47</sup> In order to obtain the total local field  $\mathbf{B}_j$  at  $\mathbf{r}_j$ , the contribution of all other dipoles has to be summed,

$$\mathbf{B}_j = \sum_{i, i \neq j} \mathbf{B}_d(\mathbf{r}_{ij}). \quad (\text{A2})$$

The local fields are calculated for all atoms within distance  $\rho$  from the  $z$  axis. The procedure of random filling of the slab and subsequent calculation of the local fields is repeated until  $10^4 - 10^5$  values are obtained. We then computed a local field probability histogram, which represents the ESR line shape  $f(B)$  in discrete intervals. The position of the  $f(B)$  peak yields the average magnetization  $B_{dip}$  in the film and the width gives the ESR line broadening due to dipolar interactions of H atoms.

We tested different lattice models: hexagonal close packed (hcp), simple cubic, and arbitrary positions of atoms. We introduced the parameter of minimum distance ( $\delta$ ) between H atoms taking into account that atoms located at neighboring lattice sites recombine and the approach of atoms toward each other has to be restricted.<sup>11,13</sup> No difference in broadening or shift was observed between different lattice types for the experimental range of densities. We also studied the dependence of the computed line shape on the minimum distance  $\delta$ . At distances larger than  $4a$  ( $a = 0.375 \text{ nm}$  for hcp  $p\text{-H}_2$ ), the shape of the local field distribution changed from Lorentzian to Gaussian. In the range  $2a \leq \delta \leq 4a$ , the simulated and experimentally measured line shapes converged and the simulated line shape remained Lorentzian. The simulations [presented in Figs. 9, 11, and 17(b)] were performed in an hcp lattice with  $\delta = 2.5a$ . The average magnetization  $\Delta B_{dip}$  was found to be constant for the film thicknesses  $d$  between  $4\delta$  ( $\approx 4 \text{ nm}$ ) and  $50 \text{ nm}$ . For unlike atoms the results for the density-dependent magnetization and the broadening are, respectively,  $-0.71 \text{ G}/10^{19} \text{ cm}^{-3}$  and  $0.85 \text{ G}/10^{19} \text{ cm}^{-3}$ .

In Figs. 9 and 11, we present results for the ESR linewidth and shift obtained in the simulations. Because the experimental line contains other sources of broadening, not included in the simulation, the widths of the simulated and experimental line shapes are not directly comparable. The experimental ESR linewidth suggests that the ESR line is broadened by two distinct sources: the density-dependent dipolar broadening due to H atoms and the constant broadening caused by other sources, containing instrumental and  $\text{o-H}_2$  contributions. With this assumption, we compared the density-dependent change in the linewidth between simulation and the experiment. The slope of the linear line in Fig. 9

is obtained from the density dependence of the  $f(B)$  width while the zero density offset is from the experiment.

To compare the simulated and experimental line shapes directly, we convoluted the simulated dipolar line shape  $f(B)$

with an experimental line shape recorded at the low density, where the dipolar broadening due to H atoms is negligible ( $n=6 \times 10^{17} \text{ cm}^{-3}$  and FWHM  $\approx 0.6 \text{ G}$ ). The result is presented in Fig. 17(b).

\*jmiaho@utu.fi

- <sup>1</sup>A. P. Bass and H. P. Broida, *Formation and Trapping of Free Radicals* (Academic, New York, 1960).
- <sup>2</sup>A. F. Andreev and I. M. Lifshitz, *Sov. Phys. JETP* **29**, 1107 (1969).
- <sup>3</sup>E. Kim and M. H. W. Chan, *Science* **305**, 1941 (2004).
- <sup>4</sup>P. W. Anderson, *Science* **324**, 631 (2009).
- <sup>5</sup>J. Ahokas, J. Järvinen, V. V. Khmelenko, D. M. Lee, and S. Vasiliev, *Phys. Rev. Lett.* **97**, 095301 (2006).
- <sup>6</sup>J. Järvinen, J. Ahokas, and S. Vasiliev, *J. Low Temp. Phys.* **147**, 579 (2007).
- <sup>7</sup>J. Ahokas, O. Vainio, J. Järvinen, V. V. Khmelenko, D. M. Lee, and S. Vasiliev, *Phys. Rev. B* **79**, 220505(R) (2009).
- <sup>8</sup>Y. Kagan and L. A. Maksimov, *Sov. Phys. JETP* **57**, 459 (1983).
- <sup>9</sup>Y. Kagan and A. J. Leggett, *Quantum Tunneling in Condensed Media* (North-Holland, Amsterdam, 1992).
- <sup>10</sup>A. V. Ivliev, A. Y. Katunin, I. I. Lukashevich, V. V. Sklyarevskii, V. V. Suraev, V. V. Filippov, N. I. Filippov, and V. A. Shevtsov, *Sov. Phys. JETP* **62**, 1268 (1985).
- <sup>11</sup>V. Shevtsov, A. Frolov, I. Lukashevich, E. Ylinen, P. Malmi, and M. Punkkinen, *J. Low Temp. Phys.* **95**, 815 (1994).
- <sup>12</sup>T. Kumada, S. Mori, T. Nagasaka, J. Kumagai, and T. Miyazaki, *J. Low Temp. Phys.* **122**, 265 (2001).
- <sup>13</sup>T. Kumada, M. Sakakibara, T. Nagasaka, H. Fukuta, J. Kumagai, and T. Miyazaki, *J. Chem. Phys.* **116**, 1109 (2002).
- <sup>14</sup>T. Kumada, *Phys. Rev. B* **68**, 052301 (2003).
- <sup>15</sup>E. B. Gordon, A. A. Pel'menev, O. F. Pugachev, and V. V. Khmelenko, *JETP Lett.* **37**, 282 (1983).
- <sup>16</sup>R. W. H. Webeler, *J. Chem. Phys.* **64**, 2253 (1976).
- <sup>17</sup>M. Sharnoff and R. V. Pound, *Phys. Rev.* **132**, 1003 (1963).
- <sup>18</sup>G. W. Collins, J. L. Maienschein, E. R. Mapoles, R. T. Tsugawa, E. M. Fearon, P. C. Souers, J. R. Gaines, and P. A. Fedders, *Phys. Rev. B* **48**, 12620 (1993).
- <sup>19</sup>G. Rosen, *J. Chem. Phys.* **65**, 1735 (1976).
- <sup>20</sup>C. K. Jen, S. N. Foner, E. L. Cochran, and V. A. Bowers, *Phys. Rev.* **112**, 1169 (1958).
- <sup>21</sup>R. K. Leach, Ph.D. thesis, University of Wisconsin, 1972.
- <sup>22</sup>I. F. Silvera and J. T. M. Walraven, *Progress in Low Temperature Physics*, edited by D. F. Brewer (North-Holland, Amsterdam, 1986), Vol. X.
- <sup>23</sup>I. F. Silvera, *Phys. Rev. B* **29**, 3899 (1984).
- <sup>24</sup>K. E. Kürten and M. L. Ristig, *Phys. Rev. B* **31**, 1346 (1985).
- <sup>25</sup>J. Helffrich, M. Maley, M. Krusius, and J. C. Wheatley, *J. Low Temp. Phys.* **66**, 277 (1987).
- <sup>26</sup>R. Van Rooijen, J. J. Berkhout, B. Hebral, and J. T. M. Walraven (unpublished).
- <sup>27</sup>S. Vasilyev, J. Järvinen, E. Tjukanoff, A. Kharitonov, and S. Jaakkola, *Rev. Sci. Instrum.* **75**, 94 (2004).
- <sup>28</sup>S. S. Rosenblum, W. A. Steyert, and F. R. Fickett, *Cryogenics* **17**, 645 (1977).
- <sup>29</sup>C. P. Slichter, in *Principles of Magnetic Resonance*, edited by P. Fulde (Springer-Verlag, Berlin, 1990).
- <sup>30</sup>C. P. Poole, *Electron Spin Resonance. A comprehensive Treatise on Experimental Techniques* (Interscience, Wiley, New York, 1967).
- <sup>31</sup>J. Ahokas, J. Järvinen, G. V. Shlyapnikov, and S. Vasiliev, *Phys. Rev. Lett.* **101**, 263003 (2008).
- <sup>32</sup>F. J. Adrian, *J. Chem. Phys.* **32**, 972 (1960).
- <sup>33</sup>L. Kevan and L. D. Kispert, *Electron Spin Double Resonance Spectroscopy* (Wiley, New York, 1976).
- <sup>34</sup>Manufactured by International Crystal Manufacturing Co.
- <sup>35</sup>L. Bruschi, G. Delfitto, and G. Mitsura, *Rev. Sci. Instrum.* **70**, 153 (1999).
- <sup>36</sup>P. Leiderer and U. Albrecht, *J. Low Temp. Phys.* **89**, 229 (1992).
- <sup>37</sup>Macroscopically thick H<sub>2</sub> films were successfully deposited by vapor condensation in similar experiments, J. Järvinen *et al.* (unpublished).
- <sup>38</sup>Y. M. Xiao, S. Buchman, L. Pollack, D. Kleppner, and T. J. Greytak, *Phys. Rev. B* **48**, 15744 (1993).
- <sup>39</sup>T. Kumada, H. Inagaki, T. Nagasawa, Y. Aratono, and T. Miyazaki, *Chem. Phys. Lett.* **251**, 219 (1996).
- <sup>40</sup>G. W. Collins, P. C. Souers, F. Magnotta, E. R. Mapoles, and J. R. Gaines, *Phys. Rev. B* **53**, 8143 (1996).
- <sup>41</sup>H. Meyer, *Can. J. Phys.* **65**, 1453 (1987).
- <sup>42</sup>J. H. Van Vleck, *Phys. Rev.* **74**, 1168 (1948).
- <sup>43</sup>A. Abragam, *Principles of Nuclear Magnetism* (Oxford University Press, New York, 1961), p. 104.
- <sup>44</sup>A. S. Iskovskikh, A. Y. Katunin, I. I. Lukashevich, V. V. Sklyarevskii, and V. A. Shevtsov, *JETP Lett.* **42**, 30 (1985).
- <sup>45</sup>I. Svare and G. Seidel, *Phys. Rev.* **134**, A172 (1964).
- <sup>46</sup>I. Shinkoda and W. N. Hardy, *J. Low Temp. Phys.* **85**, 99 (1991).
- <sup>47</sup>G. Van Gorp and A. Stesmans, *Phys. Rev. B* **45**, 4344 (1992).
- <sup>48</sup>N. Bloembergen, E. M. Purcell, and R. V. Pound, *Phys. Rev.* **73**, 679 (1948).
- <sup>49</sup>G. W. Parker, *Am. J. Phys.* **38**, 1432 (1970).
- <sup>50</sup>T. Kumada, N. Kitagawa, T. Noda, J. Kumagai, Y. Aratono, and T. Miyazaki, *Chem. Phys. Lett.* **288**, 755 (1998).
- <sup>51</sup>A. V. Ivliev, A. Y. Katunin, I. I. Lukashevich, V. V. Sklyarevskii, V. V. Suraev, V. V. Filippov, N. I. Filippov, and V. A. Shevtsov, *JETP Lett.* **36**, 472 (1982).
- <sup>52</sup>G. W. Collins, E. M. Fearon, J. L. Maienschein, E. R. Mapoles, R. T. Tsugawa, P. C. Souers, and J. R. Gaines, *Phys. Rev. Lett.* **65**, 444 (1990).